



PERGAMON

International Journal of Solids and Structures 37 (2000) 7185–7206

INTERNATIONAL JOURNAL OF
**SOLIDS and
STRUCTURES**

www.elsevier.com/locate/ijsolstr

Mesh-free simulations of shear banding in large deformation

Shaofan Li, Wei Hao, Wing Kam Liu *

Department of Mechanical Engineering, The Technological Institute, Northwestern University, 2145 Sheridan Road, Evanston, IL 60208-3111, USA

Received 5 October 1999; in revised form 27 January 2000

Abstract

Mesh-free approximation is used in numerical simulations of strain localization under large deformation. An explicit displacement based mesh-free formulation is used in both two-dimensional and three-dimensional computations.

The spatial isotropy of mesh-free interpolant is demonstrated through the numerical example to show that mesh-free methods possess certain “mesh objectivity” that alleviates the notorious mesh-alignment sensitivity associated with numerical simulation of strain localization. It is also demonstrated in the paper that mesh-free interpolants can accurately capture finite shear deformation under large mesh distortion without recourse to special mesh design and remeshing. Moreover, curved shear band surface and multiple shear band interactions are captured in numerical simulations. © 2000 Published by Elsevier Science Ltd.

Keywords: Multiple shear band formations; Large deformation; Mesh-free methods; Mesh alignment sensitivity; Particle methods; Strain localization; Curved shear band; Viscoplasticity

1. Introduction

Strain localization problems have been extensively studied in last three decades. Nonetheless, some technical issues remain open, especially in the field of numerical simulations. The classical (local) rate-independent plasticity theory lacks intrinsic length scale, which leads to the well-known mesh dependent pathology in numerical simulations. Currently, several regularization mechanisms have been introduced to bring a length scale into the constitutive model, such as adopting rate-dependent plasticity model (Needleman, 1988; Loret and Prevost, 1990; Prevost and Loret, 1990), non-local model (Bazant et al., 1984; Bazant and Pijaudier-Cabot, 1988; Aifantis, 1984), strain gradient models (Aifantis, 1992; Zbib and Aifantis, 1992; de Borst and Pamin, 1996; de Borst and Sluys, 1991; Fleck and Hutchinson, 1993; Gao et al., 1999), and micromechanics motivated multiple scale model (e.g. Garikipati and Hughes, 1998). However, strong mesh-alignment sensitivity may still be observed in numerical simulations, when the finite element mesh size is in the same order of the length scale of the constitutive model, or larger, and usually such characteristic length is very small.

* Corresponding author. Fax: +1-847-491-3915.

E-mail addresses: sf-li@nwu.edu (S. Li), haowei@nwu.edu (W. Hao), w-liu@nwu.edu (W.K. Liu).

From computational standpoint, starting from Ortiz et al. (1987), there is a school of thought that advocate embedding discontinuous (“jump”) element, or regularized singular element, into finite element solutions to emulate the discontinuous strain/displacement field (e.g. Dvorkin, 1990; Steinmann and William, 1991; Simo et al., 1993; Oliver, 1995; Armero and Garikipati, 1996 and among others). The method has gained quite popularity in recent years. However, it would be a formidable task to apply such discontinuous element technique to complicated shear band patterns, such as the interaction between micro-shear band and macro-shear band in crystal plasticity.

Recently, mesh-free methods have been applied to numerical simulation of strain localization phenomenon. Earlier results have been reported in Li and Liu (1999a); it has been found that there are several advantages in using mesh-free methods in shear band simulations, such as the feasibility to use simple displacement-based explicit formulation while avoiding volumetric locking; “non-local interpolation” to smear discontinuous field; relief of mesh-alignment sensitivity, straightforward h -adaptivity procedure, just to name a few. The emphasis of this paper is placed on the following aspects: (1) relieving mesh-alignment sensitivity; (2) simulating shear band evolution in a large deformation process that is well into the post-bifurcation regime; (3) capturing curve shear band and shear band interactions in three-dimensional (3-D) with quasi-uniform particle distribution. Note that all of the above is achieved by using a simple explicit displacement-based computation.

The arrangement of the paper is as follows: mesh-free methods, in particular, the reproducing kernel particle method (RKPM) is reviewed in Section 2, and the constitutive model and the explicit total Lagrangian formulation in finite strain are also outlined. Section 3 discusses the relief of mesh-alignment sensitivity. The “mesh-objectivity” of the mesh-free methods is demonstrated through a model problem – the 31-hole problem. Section 4 is presenting numerical examples to show the ability of mesh-free methods to simulate large deformation process without remeshing. In Section 5, the numerical simulations of curves shear band formation and shear band interactions due to multiple cracks are discussed.

2. Formulations

2.1. Mesh-free approximation

Currently, there are several mesh-free methods used in computational mechanics, such as smoothed particle hydrodynamics (SPH) (Monaghan, 1988), element-free Galerkin (EFG) (Belytschko et al., 1996), RKPM (Jun et al., 1998; Liu et al., 1995, 1996, 1997a,b) h - p Clouds (Duarte and Oden, 1996), and mesh-free local Petrov–Galerkin (MLPG) (Atluri and Zhu, 1998), etc. The particular mesh-free method used in this paper is the RKPM. A detailed account of the method can be found in Liu et al. (1997a) and Li and Liu (1999b). The basic technical ingredients of the method are outlined below.

The basic idea of RKPM is to construct a proper kernel function such that one can approximate the function of interest through a discrete “reproducing” or “filtering” representation

$$u^h(X) = (\mathcal{K}_\rho *' u)(X) := \sum_{I \in A} \mathcal{K}_\rho(X_I - X) \Delta V_I u_I, \quad (1)$$

where $\mathcal{K}_\rho(X) := 1/\rho^n \mathcal{K}(X/\rho)$, ρ is the dilation parameter which is the measure of the support size of the kernel function, and n is spatial dimension. The RKPM kernel function is compact supported, and usually very smooth, $\mathcal{K}(X) \in C^N(\Omega)$ and $N \gg 1$. Note that the symbol $*'$ is the discrete spatial convolution in strict sense, whereas the finite element interpolation can be viewed as a spatial convolution only in the sense that the kernel function is a generalized function. Assume that in the domain Ω there is a valid particle distribution, $A := \{1, 2, \dots, NP\}$. For simplicity, in the rest of the paper, we shall simply denote $\mathcal{K}_\rho(X_I - X) \Delta V_I$ as $\mathcal{K}_I(X)$. Eq. (1) can be viewed as a nonlocal interpolation (or not a “interpolation” based

on conventional definition). In such “nonlocal interpolation” scheme, any point in the domain, including particle point, is usually covered by multiple shape functions.

The RKPM shape function is constructed as follows: each particle, $I \in A$, $A := \{1, 2, \dots, NP\}$ in the domain is associated with a shape function

$$\mathcal{H}_I(X) = \mathcal{H}(X_I - X) := \mathbf{P}\left(\frac{X_I - X}{\rho}\right) \mathbf{b}(X) \phi_\rho(X_I - X) \Delta V_I, \tag{2}$$

where $\phi(X)$ is a given window function, $X = (X_1, X_2, X_3)$, $\mathbf{P}(X)$ is the given polynomial basis, and $\mathbf{b}(X)$ is an unknown function that is determined by the following moment equations:

$$\mathbf{M}(X) \mathbf{b}(X) = \mathbf{1}, \quad \mathbf{1} = \{1, 0, \dots, 0\}^T, \tag{3}$$

where both the moment and the b-vector are parametric functions of X .

A two-dimensional (2-D) bilinear RKPM shape function, and its two first order derivatives are shown in Fig. 1. It may be noted that the first order derivatives of RKPM kernel function resembles to the so-called *mesh-free wavelet* (but not the same) constructed by Li and Liu (1999b,c). There is a subtle implication in the term, *smoothness*, used in this paper. For instance, in the above example, RKPM interpolant can only reproduce the polynomials, 1, X_1 , X_2 , and $X_1 X_2$, exactly, but it is no longer piecewise linear in shape as the bilinear FEM shape function. As shown in Fig. 2, $\mathcal{H}_I(X)$ is very smooth in shape, and, as a matter of fact, $\mathcal{H}_I(X) \in C^2(\Omega)$. A tri-linear RKPM shape function in 3-D and its three first order derivatives at a selected particle are plotted in Fig. 2. Note that even though the support size of the shape function is a rectangular box, one may find that the effective domain of the shape function is a sphere, and the effective domain of its first derivatives is two connected spherical regions. This leads to the observation that the distribution of RKPM shape function is “spatial isotropic”, which is a desirable property for certain kinds of problems such as shear band simulations. For better visualization, the first octant is taken out from the sphere region in Fig. 2(a) to show that the shape function reaches its maximum value at the position of corresponding particle, i.e. the center. In Fig. 2(b)–(d), one quadrant is taken out to see the orientation and the distribution of the three derivatives.

2.2. An explicit mesh-free Galerkin formulation

We begin with defining and describing the kinematic quantities at finite strains. Followed by the standard convention that \mathbf{x} denotes the spatial coordinate of a material point and \mathbf{X} denotes the referential coordinate of that material point, the displacement of the material point is defined as

$$\mathbf{u} := \mathbf{x} - \mathbf{X} \tag{4}$$

so are the deformation gradient, and velocity field

$$\mathbf{F} := \frac{\partial \mathbf{x}}{\partial \mathbf{X}}, \tag{5}$$

$$\mathbf{v} := \frac{\partial \mathbf{u}}{\partial t}. \tag{6}$$

In inelastic large deformation, the deformation gradient, \mathbf{F} , can be decomposed as

$$\mathbf{F} = \mathbf{F}^e \cdot \mathbf{F}^p, \tag{7}$$

where \mathbf{F}^e describes elastic deformation and rigid body rotation and \mathbf{F}^p represents inelastic deformation, in this case, viscoplastic deformation. The rate of deformation tensor, \mathbf{D} , and the spin tensor, \mathbf{W} , are the symmetry part and anti-symmetry part of spatial velocity gradient $\mathbf{L} = \dot{\mathbf{F}} \cdot \mathbf{F}^{-1}$, i.e.

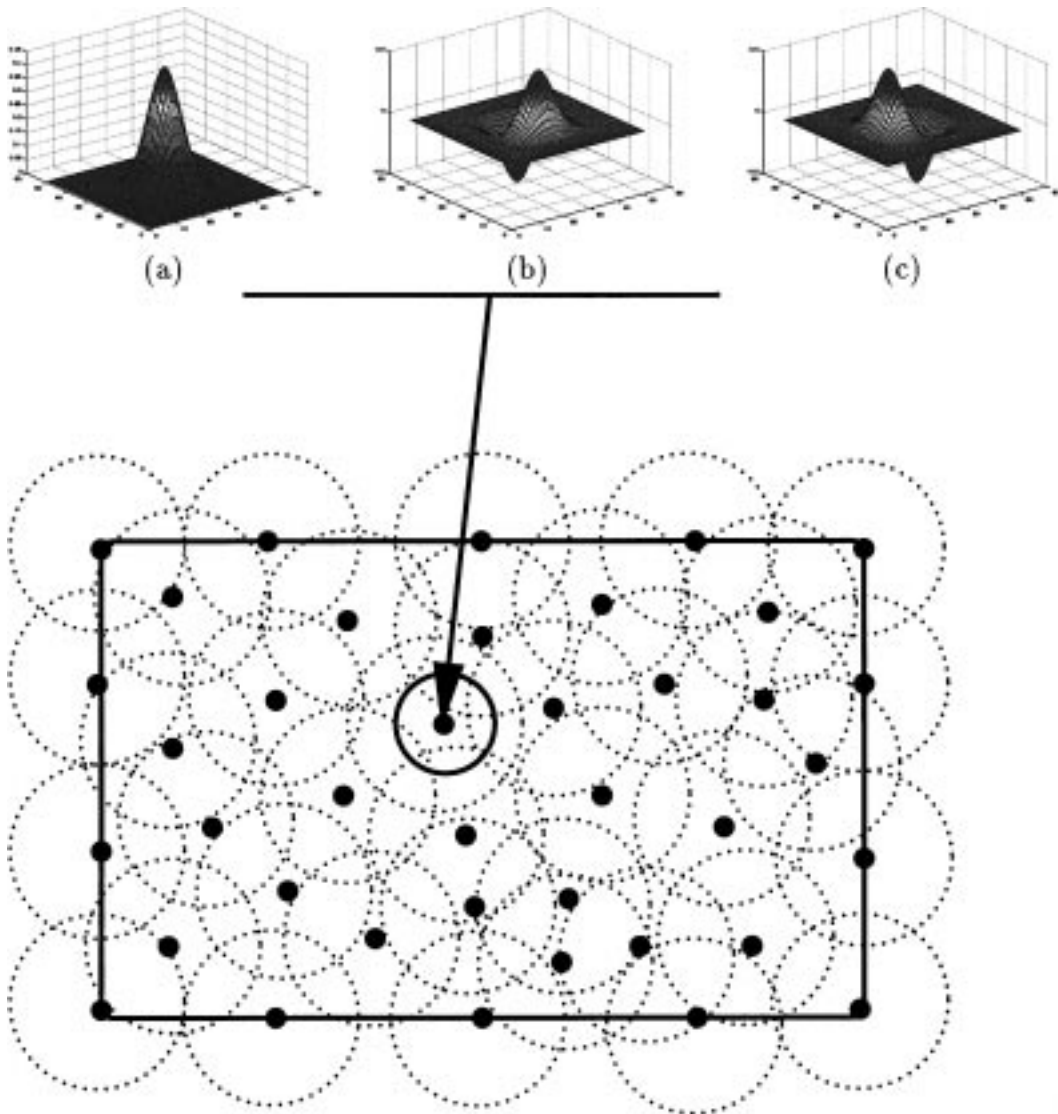


Fig. 1. 2-D RKPM shape function and its first order derivatives generated by the bilinear polynomial basis: (a) $\mathcal{H}_I(X)$, (b) $\mathcal{H}_{I,x_1}(X)$ and (c) $\mathcal{H}_{I,x_2}(X)$.

$$\mathbf{D} + \mathbf{W} = \dot{\mathbf{F}} \cdot \mathbf{F}^{-1} = \dot{\mathbf{F}}^e \cdot \mathbf{F}^{e-1} + \mathbf{F}^e \cdot \dot{\mathbf{F}}^p \cdot \mathbf{F}^{p-1} \cdot \mathbf{F}^{e-1} \quad (8)$$

with

$$\mathbf{D} := D_{ij} \mathbf{e}_i \otimes \mathbf{e}_j, \quad D_{ij} := \frac{1}{2} \left(\frac{\partial v_i}{\partial x_j} + \frac{\partial v_j}{\partial x_i} \right), \quad (9)$$

$$\mathbf{W} := W_{ij} \mathbf{e}_i \otimes \mathbf{e}_j, \quad W_{ij} := \frac{1}{2} \left(\frac{\partial v_i}{\partial x_j} - \frac{\partial v_j}{\partial x_i} \right) \quad (10)$$

and the following decomposition holds:

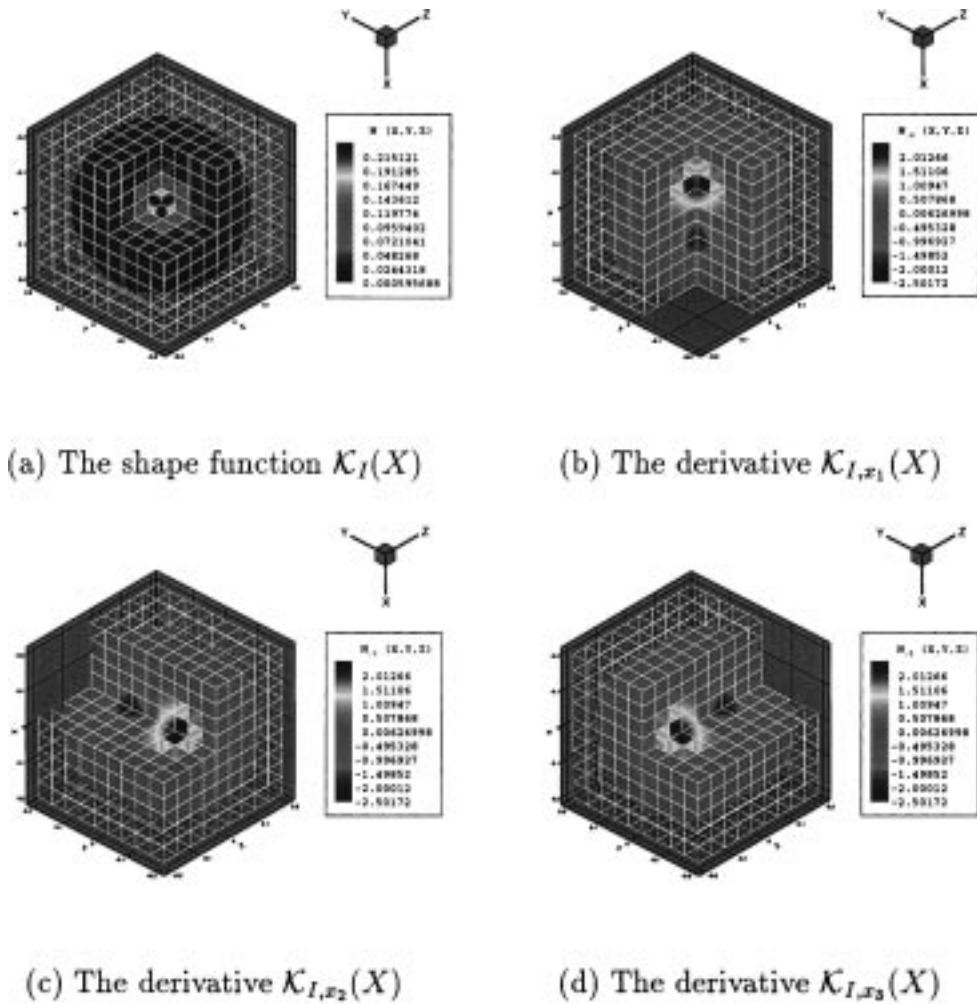


Fig. 2. 3-D RKPM shape function and its first order derivatives generated by the tri-linear polynomial basis.

$$\mathbf{D}^e + \mathbf{W}^e = \dot{\mathbf{F}}^e \cdot \mathbf{F}^{e-1}, \tag{11}$$

$$\mathbf{D}^p + \mathbf{W}^p = \mathbf{F}^e \cdot \dot{\mathbf{F}}^p \cdot \mathbf{F}^{p-1} \cdot \mathbf{F}^{e-1}. \tag{12}$$

The weak form of the balance of linear momentum can be written as

$$\int_{\Omega_0} \mathbf{P} : \delta \mathbf{F}^T d\Omega = \int_{\Omega_0} \rho_0 \mathbf{B} \cdot \delta \mathbf{u} d\Omega + \int_{\Gamma^{\text{trac}}} \mathbf{T} \cdot \delta \mathbf{u} dS - \int_{\Omega_0} \rho_0 \frac{\partial^2 \mathbf{u}}{\partial t^2} \delta \mathbf{u} d\Omega, \tag{13}$$

where \mathbf{T} is the prescribed traction on the traction boundary, Γ^{trac} , and \mathbf{P} denotes the first Piola–Kirchhoff stress tensor, which can be related to the Kirchhoff stress tensor as $\boldsymbol{\tau} = \mathbf{F} \cdot \mathbf{P}$. For simplicity, the boundary conditions are specified with respect to the referential configuration

$$\mathbf{P} \mathbf{n}_0 = \mathbf{T}^0, \quad \forall \mathbf{X} \in \Gamma_X^T, \tag{14}$$

$$\mathbf{u} = \mathbf{u}^0, \quad \forall \mathbf{X} \in \Gamma_X^u, \tag{15}$$

where $\Gamma_X^T \cup \Gamma_X^u = \partial\Omega_X$. On how to enforce the essential conditions in mesh-free implementation, readers may refer to Li and Liu (1999a).

An elasto-viscoplastic material model is adopted in computation, since the model itself is well regularized, at least in dynamic case, and the associated mathematical problem is well-posed as well (see Shawki and Clifton, 1989; (Needleman, 1988)). A rate form constitutive equation is used

$$\overset{\nabla}{\boldsymbol{\tau}} := \mathbf{C}^{\text{elas}}(\mathbf{D} - \mathbf{D}^{\text{vp}}), \quad (16)$$

where the Jaumann rate of Kirchhoff stress, $\overset{\nabla}{\boldsymbol{\tau}}$, is defined as

$$\overset{\nabla}{\boldsymbol{\tau}} = \dot{\boldsymbol{\tau}} - \mathbf{W}\boldsymbol{\tau} + \boldsymbol{\tau}\mathbf{W}. \quad (17)$$

The yield surface of viscoplastic solid is of von Mises type, which might be changing with time

$$D_{ij}^p := \bar{\eta}(\bar{\sigma}, \bar{\epsilon}) \frac{\partial f}{\partial \tau_{ij}}, \quad (18)$$

$$f(\boldsymbol{\tau}', \kappa) = \bar{\sigma} - \kappa = 0, \quad (19)$$

$$\bar{\sigma}^2 = \frac{2}{3} \boldsymbol{\tau}' : \boldsymbol{\tau}', \quad (20)$$

$$\tau'_{ij} = \tau_{ij} - \frac{1}{3} \text{tr}(\boldsymbol{\tau}) \delta_{ij}, \quad (21)$$

$$\bar{\epsilon} := \int_0^t \sqrt{\frac{2}{3} \mathbf{D}^p : \mathbf{D}^p} dt. \quad (22)$$

The power law that governs the viscoplastic flow is described as

$$\bar{\eta} = \dot{\epsilon}_0 \left[\frac{\bar{\sigma}}{g(\bar{\epsilon})} \right]^m, \quad g(\bar{\epsilon}) = \sigma_0 \frac{[1 + \bar{\epsilon}/\epsilon_0]^N}{1 + (\bar{\epsilon}/\epsilon_1)^2}. \quad (23)$$

where m is the power index.

Assume that the trial, and weight functions have the forms

$$\mathbf{u}^h(X, t) = \sum_{I \in \mathcal{A}} N_I(X) \mathbf{d}_I(t), \quad (24)$$

$$\delta \mathbf{u}^h(X, t) = \sum_{I \in \mathcal{A}} N_I(X) \delta \mathbf{d}_I(t). \quad (25)$$

The weak form (13) will lead to the following discrete equations:

$$\mathbf{M} \frac{\partial^2 \mathbf{u}^h}{\partial t^2} = \mathbf{f}^{\text{ext}} - \mathbf{f}^{\text{int}}. \quad (26)$$

The conventional row-sum lumped mass is adopted in computation, and the external and internal forces can be calculated from the following expressions:

$$\mathbf{f}_I^{\text{ext}} = \int_{\Gamma^{\text{trac}}} T_i(X, t) N_I \mathbf{e}_i dS + \int_{\Omega_0} \rho_0 B_i(X, t) N_I(X) \mathbf{e}_i d\Omega, \quad (27)$$

$$\mathbf{f}_I^{\text{int}} = \int_{\Omega_0} P_{ji}^h \frac{\partial N_I}{\partial X_j} \mathbf{e}_i d\Omega. \quad (28)$$

where \mathbf{e}_i , $i = 1, 2, 3$ are the unit vector of referential coordinate.

3. Mesh-alignment sensitivity

3.1. Opening discussion

Mesh-alignment sensitivity is a type of numerical pathology that is defined as the dependency of the finite element solution on its mesh structure, and orientation. It implies that for a same physical problem, one may get different answers, when different meshes are used. In principle, one may consider that the mesh structure is an artificial constraint, or a topological defect that is coerced subjectively onto the continuum of interests, as an additional compatibility condition. This additional mesh constraint is more than necessary as the physically required compatibility condition of the solid. In general, the usual numerical simulations of a continuous deformation process may not be susceptible to the influence of such additional constraint; however, in simulations of strain localization, mesh-alignment sensitivity becomes a major setback of finite element computation, because shear band formations always tend to form, or grow along finite element boundaries where are the places allowing possible discontinuities.

In the early studies, Tvergaard (1988) used the classic quadrilateral element (CST4) (Nagtegaal et al., 1974) in 2-D, BST24 element in 3-D to simulate strain localization, and they made an optimal arrangement of the aspect ratio of the elements, such that the real shear band formations are always aligned with the boundaries of the elements, and sharp shear bands are accurately captured in the computations. The difficulty of such matching technique is that one has to know the shear band orientation a priori. In general, both CST4 and BST24 elements show strong mesh alignment sensitivity, if the real shear band orientation is oblique to the diagonal line or plane of the quadrilateral/hexahedral element. To overcome the limitations of CST4/BST24 element, special elements have been designed to offset the undesirable mesh-alignment sensitivity. One class of such special elements are the QR4 element in 2-D and BR8 element with 1-pt. integration in 3-D. They have a relatively less dependency on spatial orientation of mesh construction, if the quadrilateral is a square, or the brick element is a square box, because they have relatively high isotropy in space. These elements are very simple and useful elements in practice, which are responsible for many successful computations in both 2-D and 3-D simulations (e.g. Watanabe et al., 1998; Zbib and Jubran, 1992), and their ability to capture the curved shear band has been reported in Batra and Stevens (1998). On the other hand, as pointed out in Li and Liu (1999a), they suffer setbacks in h -adaptivity, and lack of accuracy in post-bifurcation regime.

Another class of elements are the discontinuous (singular) elements, which can eliminate mesh alignment sensitivity for arbitrary mesh arrangement, and they usually come as incompatible modes with corresponding mixed formulations. In practice it may be difficult to implement them in complicated situations, such as large deformation process that is well into the post-bifurcation regime. From this perspective, available remedies for mesh-alignment sensitivity are either too complex, or too ad hoc and limited in general purposes.

3.2. The 31-hole problem

The purpose of this example is to demonstrate or to compare mesh-alignment sensitivity in simulations of strain localization via finite element methods and via mesh-free methods. The original 31-hole problem is proposed by Al-Ostaz and Jasiuk (1997), who studied the crack initiation and propagation in elastic-brittle and ductile thin sheets. The so-called 31-hole problem is: a square plate with 31 randomly distributed holes under tension in vertical direction. Obviously, this proposal has its micromechanics implication. The 31-hole plate used in our simulation is a 3.3 mm \times 3.3 mm square slab (plane strain), and all 31 holes have the same size, i.e., 0.25 mm in diameter. On the top and the bottom surfaces of the slab, a velocity boundary condition is prescribed by a magnitude of 10 ms⁻¹ as shown in Fig. 3 (a prescribed traction condition is used in Al-Ostaz and Jasiuk (1997)).

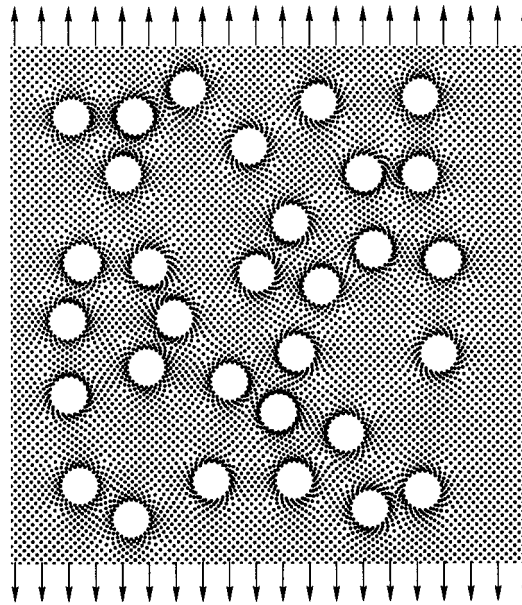


Fig. 3. The plate with 31 holes under uniaxial tension.

The material model of the plate is the power law governed elasto-viscoplastic material described in Section 2, with hardening parameters, $m = 100$, $n = 0.1$, and material constants: $E = 2.11$ GPa, $\nu = 0.3$, $\sigma_0 = 460.0$ MPa, $\dot{\epsilon}_0 = 2.0 \times 10^{-3} \text{ s}^{-1}$, $\epsilon_0 = 2.18 \times 10^{-3}$, $\epsilon_1 = 100\epsilon_0$.

The first set of computations are carried out using uniform (in an average sense) mesh/particle distributions. The plate is discretized into three different meshes/particle distributions: 40×40 , 60×60 , and 80×80 , element/cell. In FEM calculations, CST4 element is used; an additional nodal point is inserted at the center of the quadrilateral element to form the four triangular elements. With the ‘averagely’ uniform mesh/particle-distribution, the finite element method (CST4) and the mesh-free method (RKPM) give almost identical results on shear band formation; at least, the main features of the shear band formation are the same. As the mesh/particle distribution is refined from 40×40 to 80×80 element/cell, the numerical solutions seem to converge as shown in Fig. 4. From Fig. 4, one may find that the main shear band paths in both FEM calculation and RKPM calculation are very similar, or almost exactly the same in the lower part. They are also very similar to the crack propagation pattern in a FEM calculation carried out by Al-Ostaz and Jasiuk (1997) using the maximum in-plane normal principal stress criterion for an elastic-brittle material. And it is one of the possible crack paths suggested by experiments, though the exact geometry, and material conditions are not exactly the same between this simulation and that of Al-Ostaz and Jasiuk (1997).

In the second set of tests, instead of using uniform discretization, non-uniform refinements are used in computations to compare FEM and RKPM performance. Three meshes/particle distributions are chosen: 60×60 , 60×90 and 90×60 element/cell. In the 60×60 element/cell discretization, the numerical results from both FEM and RKPM are virtually just discussed. Now we examine the effect of non-uniform discretization. We refine the mesh in the vertical direction, and use a 60×90 element/cell mesh. In this case, the spatial aspect ratio of the quadrilateral element changes from 1:1 to 1.5:1.0, which means for FEM mesh the shape of quadrilateral element change from a square to a rectangle. Comparing the numerical results between FEM and RKPM, one may find that the shear band formation changes its path in FEM computation, whereas the main features of the numerical solution obtained in RKPM computation remain

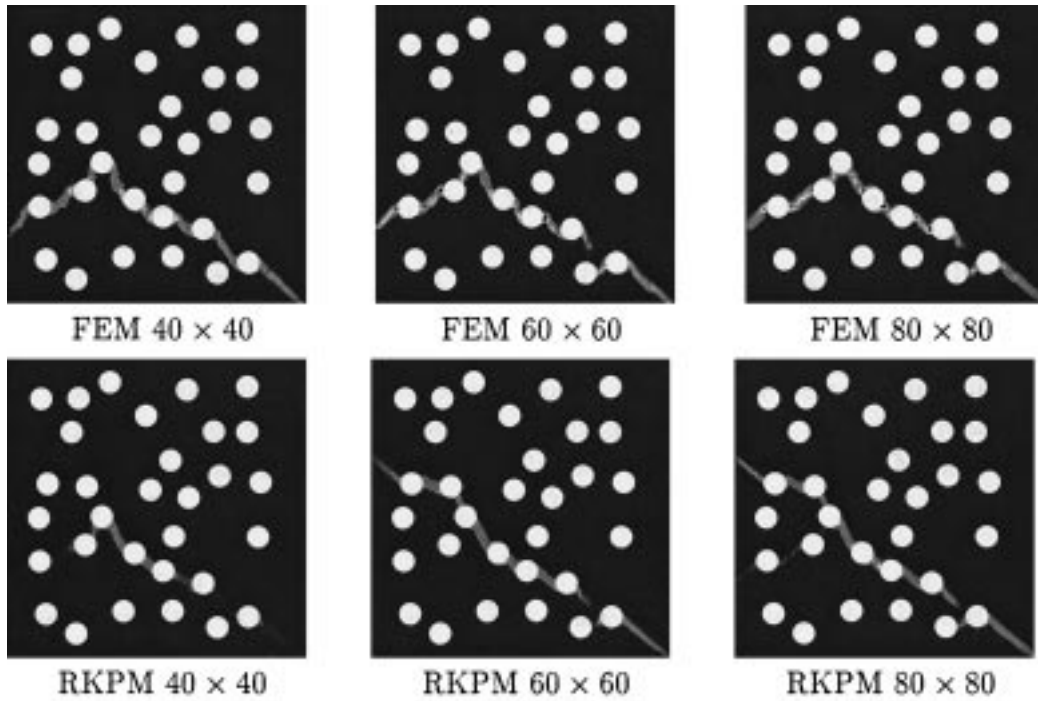


Fig. 4. Numerical results obtained via FEM and RKPM with quasi-uniform spatial aspect ratios in mesh/particle distribution.

almost the same as before. Next, we alternate the refinement direction from the y direction to the x direction such that a 90×60 element/cell mesh is used. As expected, the shear band formation changes its course again in this case, and it has a different pattern from the previous two patterns, whereas the main shear band pattern in RKPM computation remain unchanged, though a secondary branch become visible.

A quantitative comparison in the load–deflection paths is made between the finite element computation and the mesh-free computation. The comparison results are depicted in Fig. 5, from which, one may find

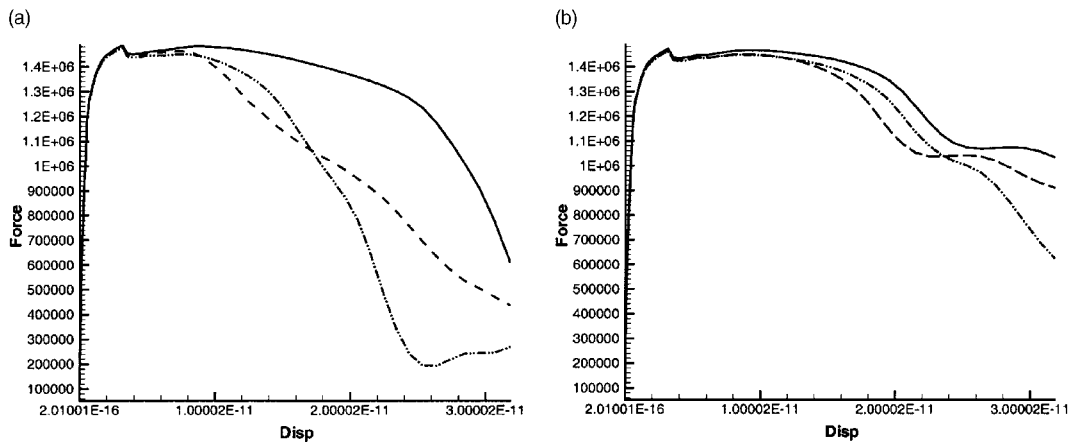


Fig. 5. The load–deflection path: (a) FEM, (b) RKPM; (solid line: 60×60 , dash-dotted line: 60×90 , dashed line: 90×60).

that the load–deflection curves in the case of mesh-free method (RKPM) are much closer in all three different particle distributions than their counterparts of finite element (FEM) calculation. It is a clear demonstration of the mesh-free method’s ability to alleviate the mesh alignment sensitivity, though, as shown in Fig. 5, the mesh alignment sensitivity is not completely eliminated in mesh-free (RKPM) computation, needless to say in FEM computation.

It should be noted, however, the shear band path in 90×60 FEM mesh is very similar to the one of plastic deformation pattern in experiments (Al-Ostaz and Jasiuk, 1997; Fig. 20) (in experiments both paths have appeared with different specimens), which might be a valid physical solution, nonetheless, RKPM solution captured the same feature as well without losing the main path of the shear band formation.

From the nodal particle distribution point of view, after all, the finite element calculation and mesh-free calculation share almost the same particle distribution, except for finite element calculation, there is an additional nodal point inside each quadrilateral element. The key technical element here is the so-called “mesh objectivity”. We define “the mesh objectivity”, or “particle distribution objectivity” as: the shape of the compact support for mesh-free interpolants is independent from the density of particle distribution.

More specifically, the compact support of mesh-free interpolant is free of any constraint set by the “spatial aspect ratio” of the particle distribution, the user has extra freedom to adjust the shape as well as the size of the compact support at ones own disposal; whereas for mesh-based finite element discretization, once the nodes are distributed, the shape and the size of each element is set. To make a direct comparison, one may look closely at the region marked in Fig. 6(a). We plot the finite element meshes and mesh-free particle distributions in Fig. 7. As mentioned before, in the case of non-uniform meshes, the spatial aspect ratio of each element changes as we either refine along the vertical direction or the horizontal direction, which can be seen clearly in the upper part of Fig. 7. In the lower part of Fig. 7, the three corresponding

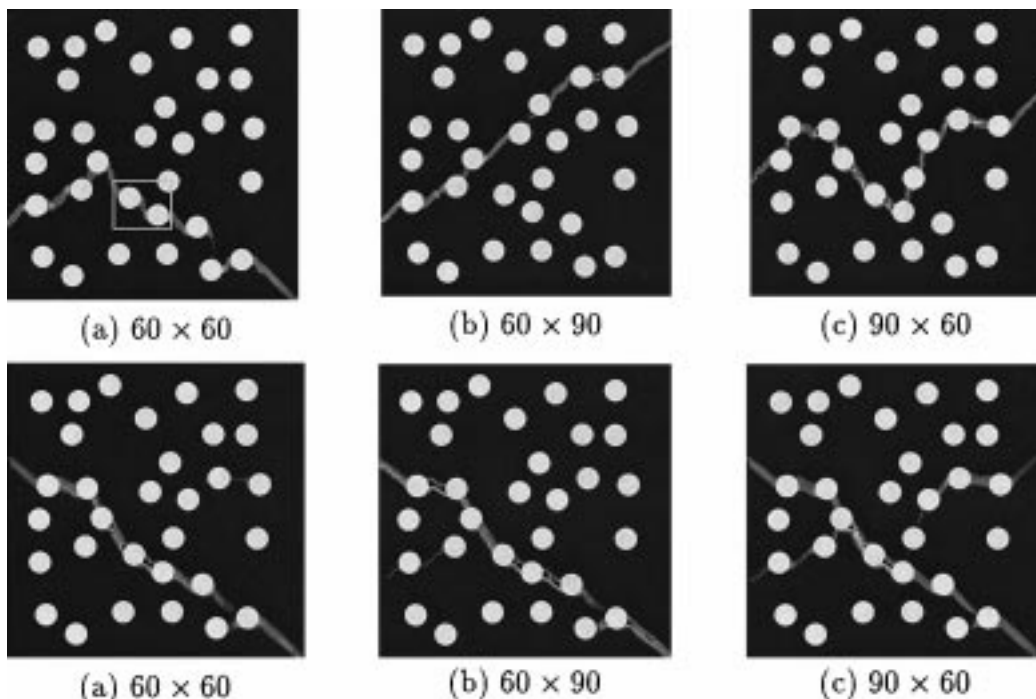


Fig. 6. Numerical results obtained via FEM and RKPM with different spatial aspect ratios in mesh/particle distribution.

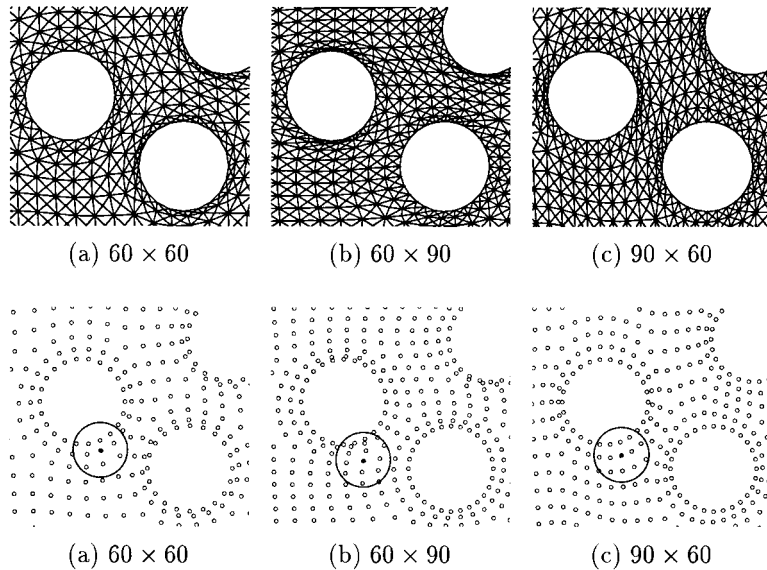


Fig. 7. Zoom-in region for different finite element meshes and mesh-free particle distributions.

mesh-free particle distributions are plotted. Note that in the mesh-free computations, we fixed the shape as well as the support size of each mesh-free shape function. Therefore, even though the particle density has changed and become non-uniform in different spatial directions, the shape and the size of compact support of RKPM shape function remain the same. As a matter of fact, the shape of the compact support is the most important factor to maintain “mesh objectivity”. As long as one uses circular compact support, or square compact support, one may achieve certain compensation over the non-uniform particle distribution, because circular or square support attains the maximum or relatively maximum spatial isotropy in two dimensional space.

4. Finite shearing in large deformation

4.1. Opening discussion

Another claimed virtue of mesh-free interpolant is its ability to endure large “mesh” distortion, and sustain computation without remeshing. Since most strain localization events are accompanied with large shear deformation, it is computationally advantageous to be able to simulate finite shearing caused by strain localization without remeshing.

The reasons that mesh-free methods can deal with extremely large deformation are twofold: variable connectivity and large support size. In practice, variable, or adjustable connectivity could be computationally expensive, because it requires new search to update the connectivity array frequently. In this paper, we restrict our attention to mesh-free discretization with fixed connectivity.

In real continua, the deformation gradient at any spatial point depends on infinite points surrounding it, thus, it is physically impossible that the deformation gradient become singular unless the material fails. In FEM approximation, the discrete deformation field within an element is determined only by a few nodal points (less than 10 in most lower order finite elements), which may lead to the degeneration of the

deformation field, i.e. singular value occurs in the deformation gradient, during computations of large deformation. Whereas in mesh-free approximation, the support size of mesh-free interpolants is much larger than the support size of finite element shape function. In 2-D, there may be 25–50 particles in a support of RKPM shape function, and in 3-D, this number increases to 100–200 particles. Because the discrete deformation field of mesh-free approximation at any spatial point is dependent on far more particles than that of the finite element approximation, the determinant of the Jacobian, i.e. the deformation gradient can maintain positive under a large mesh distortion, and consequently, the computation sustains in mesh-free approximation. Whereas in finite element approximation, the same amount mesh distortion, or less, may lead to a singular value in the Jacobian determinant, and hence terminates the computation. A schematic illustration of the support distortion of mesh-free interpolants is shown in Fig. 8.

4.2. Tension of a rectangular bar with a hole

The model example is a rectangular bar with a hole under tension (Fig. 9). Two kinematically admissible solutions (lower bound solutions) for the perfectly plastic material are shown in Fig. 10 (see: Chen and Han, 1988). One is the symmetric mode of the slip line solution, the bar splits into four rigid parts around the hole during “strong” discontinuous deformation. The other is the unsymmetric mode of the slip line solution, the bar splits into two rigid parts that drift apart from each other. Since localization of the strong

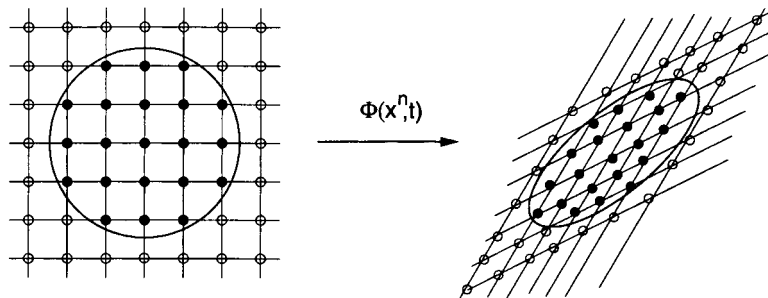


Fig. 8. The compact support of mesh-free interpolant under large distortion.

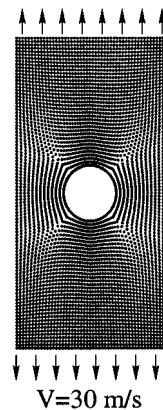


Fig. 9. The problem statement for a bar with a hole in tension.

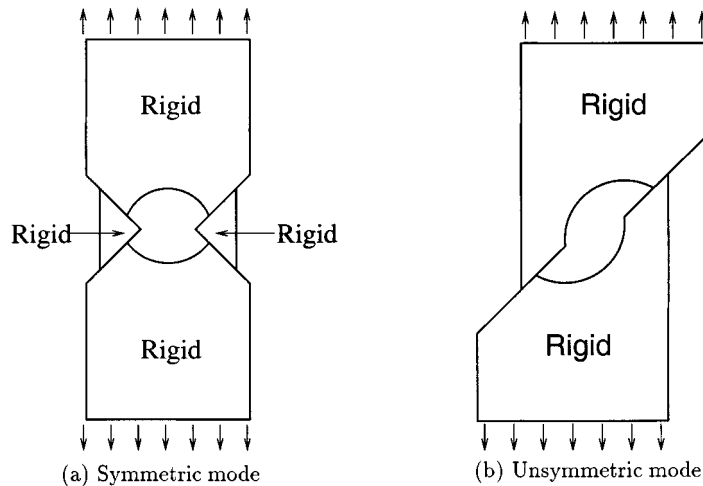


Fig. 10. Kinematically admissible deformation field for perfectly plastic material.

discontinuity may be viewed as a limit case of strain localization (weak discontinuity), one may expect some resemblance between the slip line solution and the strain localization solution, which may serve as a reality check for mesh-free simulation.

The bar is simulated as a 3-D elasto-viscoplastic solid with 4 mm in height, 2 mm in width, and 0.1 m in thickness – virtually a plane strain problem. The circular hole is penetrating through the thickness of the bar, with 0.72 mm in diameter. The prescribed velocity in upper and bottom surface of the bar is 30 ms^{-1} . In the computation, a total of 12,816 particles are used in mesh-free discretization. Three layers of particles are deployed in the thickness direction. A $2 \times 2 \times 2$ integration scheme is used to integrate the weak form. In order to trigger the unsymmetric shearing mode, a small velocity perturbation of 0.1 ms^{-1} is added on both the top and the bottom loading surface in the horizontal direction. Both symmetric solution and unsymmetric solution are displayed in Fig. 11, in which equivalent plastic strain can be visualized on top of the deformed configurations. Comparing the 3-D numerical solution of the elasto-viscoplastic solid (Fig. 11) with the 2-D slip line solution of the perfectly plastic solid (Fig. 10), one may find striking resemblance of the two, except that the shear band of the strain localization has finite width as shown in Fig. 11. Note that in Fig. 11 the coordinate aspect ratio in thickness direction has been scaled to better demonstrate the results. The deformation sequences are displayed in Fig. 13(a) for symmetric mode and in Fig. 13(b) for unsymmetric mode.

To further examine the movement of particles within the shear band, we zoom in the deformed configurations of the shear band for both shearing modes (see Fig. 12). For the sake of comparison, we first plot the deformed particle distribution within the shear band, and then we connect those particles with “mesh line” according to the background integration cell, as if it is a finite element discretization. One can see immediately that if the discretization were mesh based, the element within the shear band would have degenerated into a very thin slice, or even the opposite boundaries lay top onto each other – an indication of occurrence of singularity in deformation gradient, which would have led to early failure of the computation. Nonetheless, mesh-free methods is free of such restraint because of its relatively larger support size.

The ability of mesh-free interpolant to deal with large deformation computations is certainly not limited to the finite shearing. Fig. 14 shows a deformation of rectangular bar under uniaxial tension. The bar is 4 mm long, 2 mm in width, and 2 mm in thickness. A prescribed velocity boundary is applied on the top and bottom surface at the magnitude of 10 ms^{-1} . A total of 18,081 particles are used in the computation.

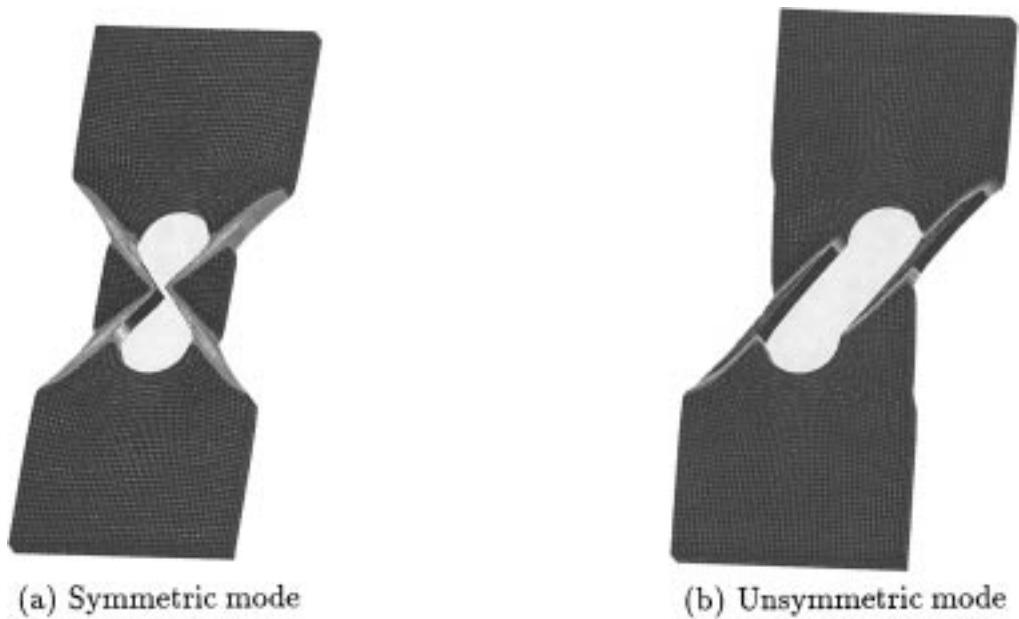


Fig. 11. Finite shearing of a 3-D elasto-viscoplastic bar.

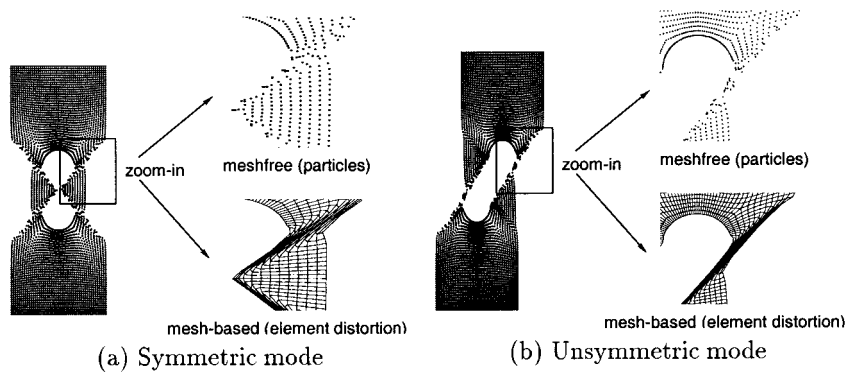


Fig. 12. The finite stretching and distortion of particle distribution within the shear band.

5. Shear band interactions due to multiple cracks

It is often considered as a challenge to capture a curved shear band formation with a uniform mesh/particle-distribution, since it does not have any special background alignment with the orientation of the incoming curved shear band. The interaction between shear bands is another severe testing problem to examine the numerical method's ability to capture shear band formation in an evolution process.

In this section, we study the shear band formations induced by cracks in 3-D case. In mesh-free discretization, when a crack is embedded into the continuum, the shape and size of the compact support of the shape functions have to be redefined. The rule for such redefinition of domain of influence for a particle, or

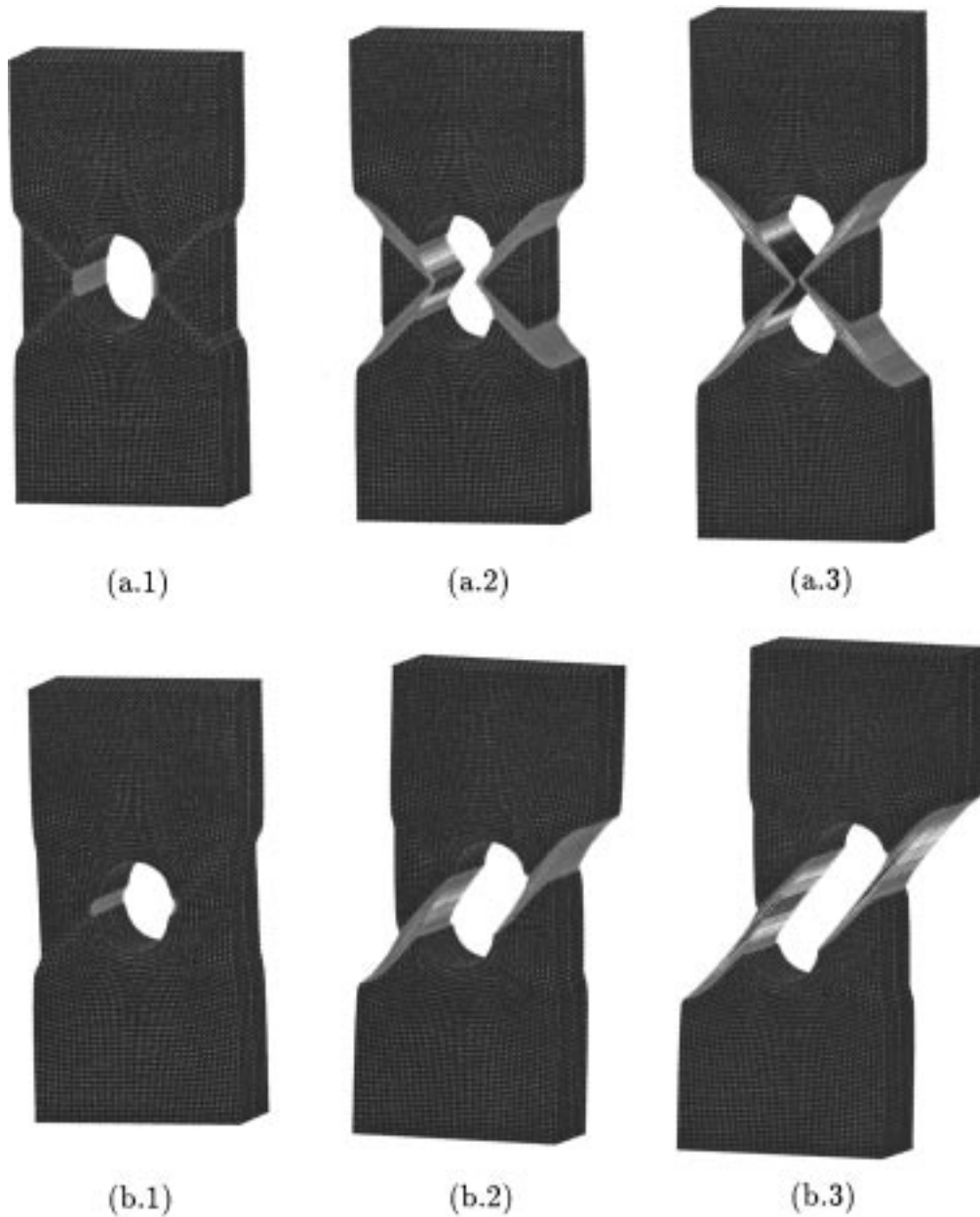


Fig. 13. Deformation sequence for a bar with a hole: (a) symmetric mode and (b) unsymmetric mode.

for any point in the domain, is the so-called “*visibility condition*” proposed by Belytschko et al. (1994). An equivalent version of the visibility condition is stated at the following. When the moment matrix in a spatial point X , $X \in \Omega$, is constructed, all the contributing particles forms a subset of particles from the particles in the original domain of influence of the point X ; such that one can connect any particle in this subset with the point X in a straight line without intercepting the boundary of the domain, for instance, the crack surfaces. In other words, we reshape the domain of influence of any point X , such that any straight line

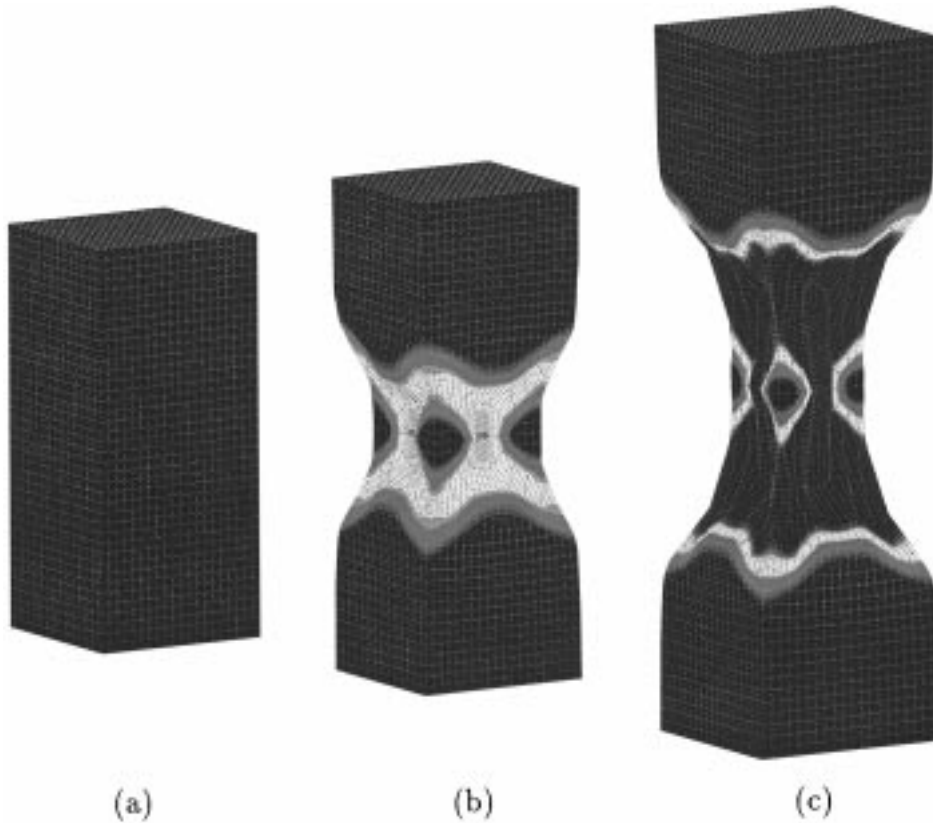


Fig. 14. Large deformation of a rectangular bar under tension.

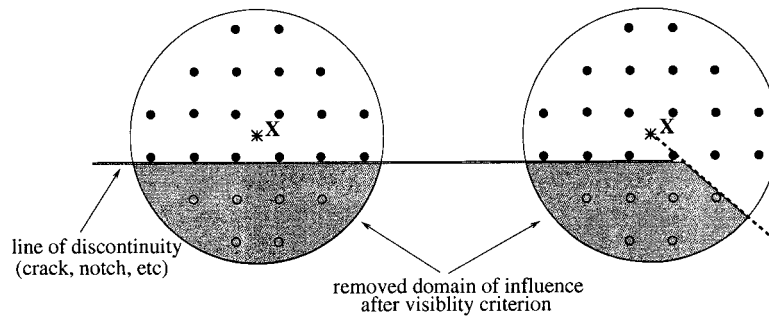


Fig. 15. The visibility criterion in determining the domain of influence of a spatial point X .

connecting the point X with a particle in its domain of influence does not penetrate crack surfaces. Fig. 15 illustrates how such modified domain of influence is being constructed. In Fig. 15, all the particles participating the construction of moment matrix at the point, X , are marked as black circle, and all the particles that are cut from the original domain of influence of the point, X , are marked with the hollow circle.

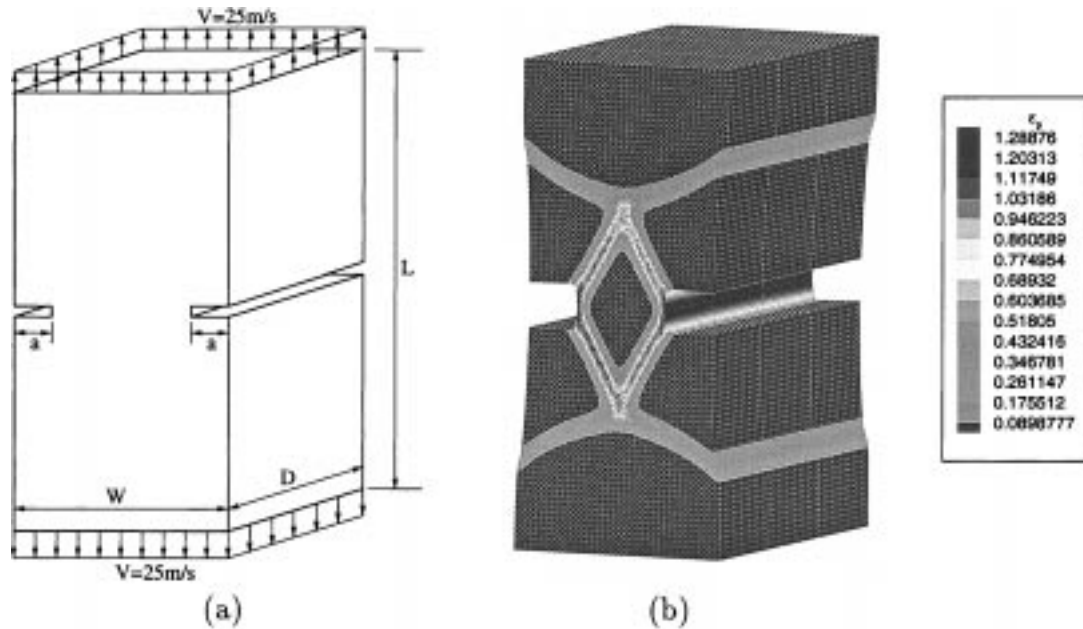


Fig. 16. The problem statement (a) and a deformed shape (b) of a double-notched block under tension.

The first example is a rectangular plate prescribed with velocity boundary conditions in the vertical direction such that the plate is in the tension state as shown in Fig. 16. The plate is 4 mm high, 2 mm in width, and 2 mm in thickness. Two edge cracks are placed in the middle of the plate with a length of 0.45 mm. Four layers of particles are deployed in the thickness direction, and a total of 13,364 particles are used in mesh-free discretization. In the explicit integration algorithm used, the time step Δt is chosen to be 1.0×10^{-9} s. The prescribed loading velocity is 25.0 ms^{-1} . A deformed shape of double-notched plate is shown in Fig. 16(b). The color contour demonstrates the intensity of the effective plastic strain. One may find that after the two shear bands pass cross each other, the outer part of the shear band becomes a cylindrical surface, or a finite cylindrical layer with non-zero curvature. The numerical result suggests that the mesh-free interpolant is insensitive to the alignment of the particle distribution, or the mesh-free interpolant may capture the natural evolution process of the shear band by avoiding the unphysical influence from the artificial structure of the mesh, or particle distribution. It should be noted that the shear band pattern obtained here is similar to the slip line solution obtained by Ewing and Hill (1967) under the plane strain condition, though in Ewing–Hill solution (Fig. 17), the inner part of the shear band is curved, whereas the outer part of the shear band is straight. The discrepancy between mesh-free solution and Ewing–Hill slip line solution may be due to the difference in material modeling, as well as the difference between strong discontinuous solution and strain localization solution.

The second example is a plate with four penetrating cracks: two edge cracks and two interior cracks as shown in Fig. 18. In this case, there are six pre-notched crack fronts; each crack front will generate a pair of shear bands. Thus the global failure mode could be an outcome of the interactions of these twelve distinct shear bands. In the interaction process, some shear bands will outlast the others, and others may disappear, depending on many different factors, such as the size, and spatial aspect ratio of the plate, the size and location of the cracks, and external loading conditions, etc. In general, it is difficult to make an accurate prediction of the global failure mode and the precise discontinuous field in the evolution process because the interactions among shear bands could be complicated for real materials, such as the

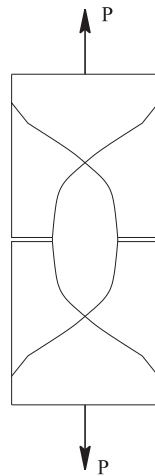


Fig. 17. The slip line solution for perfectly plasticity material by Ewing and Hill.

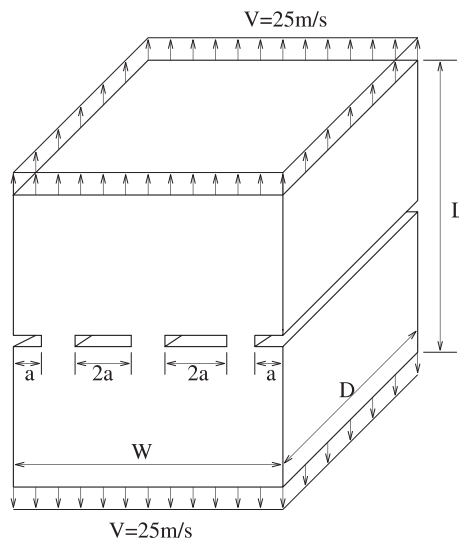


Fig. 18. The problem statement for a block with four crack under uniaxial tension.

elasto-viscoplastic model used in this computation. A sequence of shear band evolution process is shown Fig. 20(a).

In the numerical simulation, the computation specimen used in computation is 4 mm in length, 4.2 mm in width, 40 mm in thickness. The full length of a crack is $2a$, $a = 0.25$ mm; and two edge cracks are only at half length. Four layers of particles are distributed along thickness direction, and a total 27,676 particles are uniformly distributed within the four layers. The prescribed velocity at both top and bottom surfaces are 25 m s^{-1} .

In Fig. 19, the shear band interaction patterns are shown at two different time instance in plane view. One may find that in this particular case that in early stage the twelve shear bands are all initiated at the

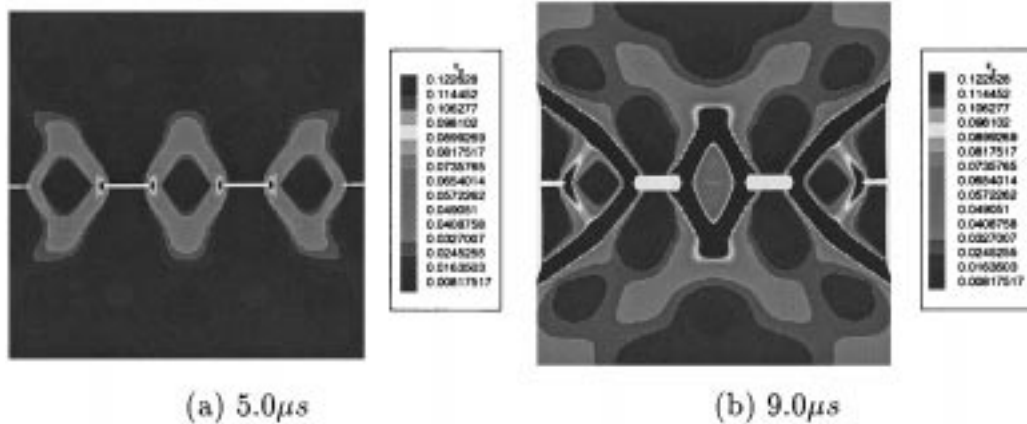


Fig. 19. Global shear band formations of a plate with four cracks at different time steps (plane view).

beginning, and have same intensity Fig. 19(a). As the deformation goes on, the shear bands generated by the interior cracks have more thrust than the shear bands generated by the edge cracks, and those shear bands are suppressed for further progress. A complete sequence of the shear band interaction in this case is shown in Fig. 20(b).

From Fig. 20(b), one may observe that the two center cracks first grow vertically, and then expand becoming two holes, or voids in the middle of the plate, and eventually the two voids coalesce and the two separated shear band emerge into an intense shear deformation zone in the middle of the two voids. This is a typical case that the approach that is embedding discontinuous element into finite element solution will have troubles to deal with, because of the changing pattern of shear band formations.

6. Concluding remarks

In this paper, mesh-free discretization/approximation is used with a simple explicit displacement based formulation to simulate both 2-D and 3-D shear formations under large deformation. The main technique merits of such mesh-free explicit formulation are: (1) its non-local character in approximation might have helped the strain localization computation as being a “numeric agent” to smear possible discontinuous fields, or to “regularize” the discrete algebraic system; (2) the large support size of mesh-free interpolants allows mesh-free computation sustain under large mesh/particle distribution distortion; (3) the window based mesh-free interpolant is a very smooth interpolation, and in principle, one may increase the smoothness of the interpolation without increasing the total degrees of freedom. Such smoothness may help the displacement based formulation to avoid volumetric locking without using mixed formulation, or one may adopt “reduced” quadrature integration without incurring rank deficiency, while relieve volumetric locking. In addition, it has shown in the paper that the numerical results based on mesh-free interpolation is insensitive to particle distribution, because of the spatial isotropy that mesh-free interpolant enjoys, which provide a much needed particle distribution objectivity for the computation, and effectively relieve the mesh-alignment sensitivity that conventional finite element methods suffered in numerical simulations of strain localization.

In summary, the mesh-free approach is simple, viable, and robust, and it shows much potential in capturing curved shear band formations, as well as accurately predict complicated shear band interaction

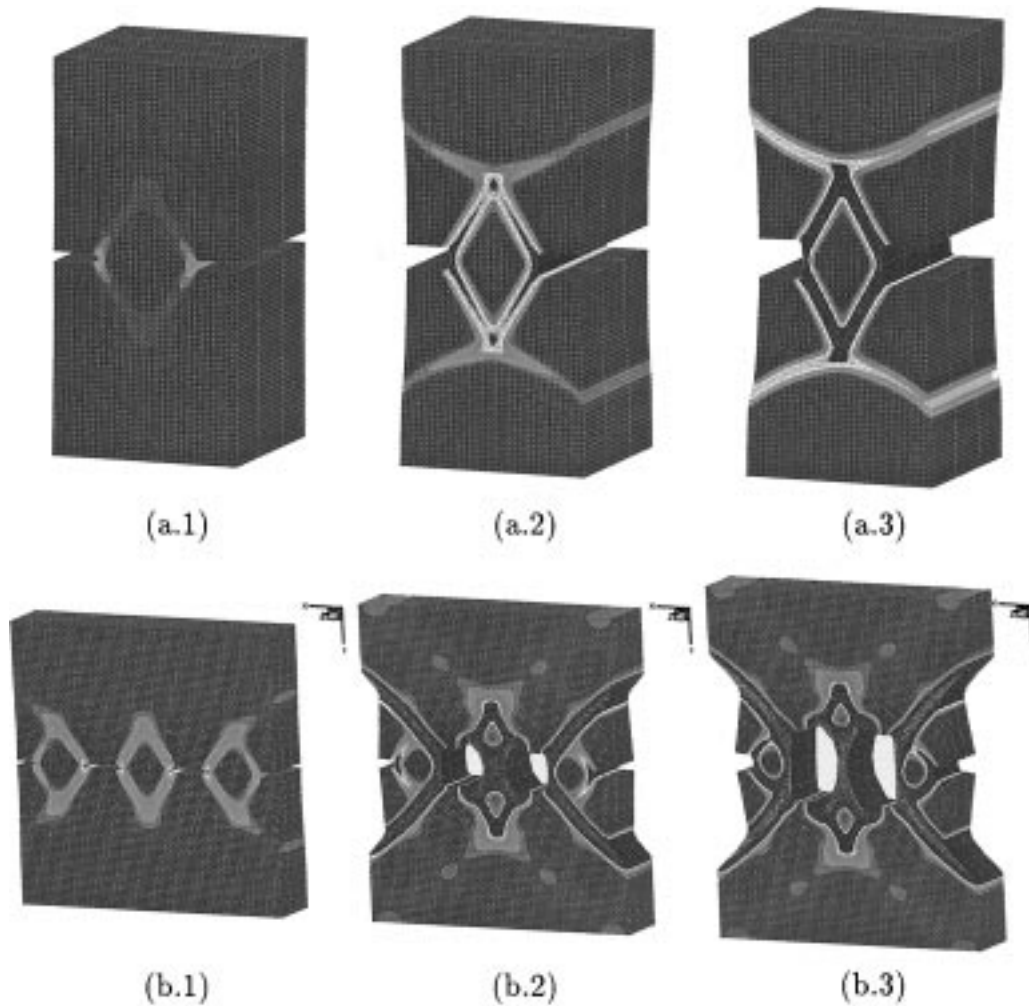


Fig. 20. Deformation sequences for shear band interaction due to multiple cracks: (a) double edge crack specimen; (b) four crack specimen.

patterns. The actual computations presented in this paper are computed by using a 2-D, and a 3-D explicit, dynamic, mesh-free codes, *dyme2d* and *dyme3d*, which are developed by the first author.

Acknowledgements

The authors would like to thank Dr. Kent T. Danielson at US Army Engineer Waterways Experiment Station, and Dr. Aziz Uras at Argonne National Laboratory, who are responsible for developing the parallel version of *dyme3d* code that has been used in the computation of this work. This work is supported by grants from the Army Research Office, and National Science Foundations. It is also sponsored in part by the Army High Performance Computing Research Center under the auspices of the Department of the Army, Army Research Laboratory cooperative agreement number DAAH04-95-2-003/contract number

DAAH04-95-C-0008, the content of which does not necessarily reflect the position or the policy of the government, and no official endorsement should be inferred.

References

- Aifantis, E.C., 1984. On the microstructural origin of certain inelastic model. *International Journal of Engineering Material Technology* 106, 326–330.
- Aifantis, E.C., 1992. On the role of gradients in the localization of deformation and fracture. *International Journal of Engineering Science* 30, 1279–1299.
- Al-Ostaz, A., Jasiuk, I., 1997. Crack initiation and propagation in materials with randomly distributed holes. *Engineering Fracture Mechanics* 58, 395–420.
- Armero, F., Garikipati, K., 1996. An analysis of strong discontinuities in multiplicative finite strain plasticity and their relation with the numerical simulation of strain localization in solid. *International Journal of Solids and Structures* 33, 2863–2885.
- Atluri, S.N., Zhu, T., 1998. A new mesh-free local Petrov–Galerkin (MLPG) approach in computational mechanics. *Computational Mechanics* 22, 117–127.
- Batra, R.C., Stevens, J.B., 1998. Adiabatic shear bands in axisymmetric impact and penetration problems. *Computer Methods in Applied Mechanics and Engineering* 151, 325–342.
- Bazant, Z.P., Belytschko, T., Chang, T.P., 1984. Continuum theory for strain-softening. *ASCM Journal of Engineering Mechanics* 110, 1666–1691.
- Bazant, Z.P., Pijaudier-Cabot, G., 1988. Nonlocal continuum damage localization instability and convergence. *Journal of Applied Mechanics* 55, 287–293.
- Belytschko, T., Lu, Y.Y., Gu, L., 1994. Element free Galerkin methods. *International Journal for Numerical Methods in Engineering* 37, 229–256.
- Belytschko, T., Krongauz, Y., Organ, D., Fleming, M., Krysl, P., 1996. Meshless methods: an overview and recent developments. *Computer Methods in Applied Mechanics and Engineering* 139, 3–48.
- Chen, W.F., Han, D.J., 1988. *Plasticity for Structural Engineers*. Springer, New York.
- Borst, R., Pamin, J., 1996. Some novel developments in finite element procedures for gradient-dependent plasticity. *International Journal for Numerical Methods in Engineering* 39, 2477–2505.
- Borst, R., Sluys, L.J., 1991. Localization in a cosserate continuum under static and loading conditions. *Computer Methods in Applied Mechanics and Engineering* 90, 805–827.
- Duarte, C.A., Oden, J.T., 1996. Hp clouds – an hp meshless method. *Numerical Methods in Partial Differential Equations* 12, 673–705.
- Dvorkin, E.N., 1990. Finite elements with displacement interpolated embedded localization lines insensitive to mesh size and distortions. *International Journal for Numerical Methods in Engineering* 30, 541–564.
- Ewing, D.J.F., Hill, R., 1967. The plastic constraint of V-notched tension bars. *Journal of the Mechanics and Physics in Solids* 15, 115–124.
- Fleck, N., Hutchinson, J., 1993. A phenomenological theory for strain gradient effects in plasticity. *Journal of Mechanics and Physics in Solids* 41, 1852–1857.
- Gao, H., Huang, Y., Nix, W.D., Hutchinson, J.W., 1999. Mechanism-based strain gradient plasticity I. Theory. *Journal of Mechanics and Physics of Solids* 47, 1239–1263.
- Garikipati, K., Hughes, T.J.R., 1998. A study of strain localization in a multiple scale framework – the one-dimensional problem. *Computer Methods in Applied Mechanics and Engineering* 59, 193–222.
- Jun, S., Liu, W.K., Belytschko, T., 1998. Explicit reproducing kernel particle methods for large deformation problems. *International Journal for Numerical Methods in Engineering* 41, 137–166.
- Li, S., Liu, W.K., 1999a. Numerical simulations of strain localization in inelastic solids using mesh-free methods. *International Journal of Numerical Methods for Engineering* 48, 1285–1309.
- Li, S., Liu, W.K., 1999b. Reproducing kernel hierarchical partition of unity part I: formulation & theory. *International Journal for Numerical Methods in Engineering* 45, 251–288.
- Li, S., Liu, W.K., 1999c. Reproducing kernel hierarchical partition of unity part II: applications. *International Journal for Numerical Methods in Engineering* 45, 288–317.
- Liu, W.K., Jun, S., Zhang, S., 1995. Reproducing kernel particle methods. *International Journal of Numerical Methods in Fluids* 20, 1081–1106.
- Liu, W.K., Chen, Y., Uras, R.A., Chang, C.T., 1996. Generalized multiple scale reproducing kernel particle methods. *Computer Methods in Applied Mechanics and Engineering* 139, 91–158.
- Liu, W.K., Li, S., Belytschko, T., 1997a. Moving least square reproducing kernel method part I: methodology and convergence. *Computer Methods in Applied Mechanics and Engineering* 143, 422–433.

- Liu, W.K., Uras, R.A., Chen, Y., 1997b. Enrichment of the finite element method with reproducing kernel particle method. *ASME Journal of Applied Mechanics* 64, 861–870.
- Loret, B., Prevost, J., 1990. Dynamic strain localization in elasto- (visco-) plastic solids, part I: general formulation and one-dimensional examples. *Computer Methods in Applied Mechanics and Engineering* 83, 247–273.
- Monaghan, J.J., 1988. An introduction to SHP. *Computation Physics Communication* 48, 89–96.
- Nagtegaal, J.C., Parks, D.M., Rice, J.R., 1974. On numerical accurate finite element solutions in the fully plastic range. *Computer Methods in Applied Mechanics and Engineering* 4, 153–177.
- Needleman, A., 1988. Material rate dependent and mesh sensitivity in localization problems. *Computer Methods in Applied Mechanics and Engineering* 67, 68–85.
- Oliver, J., 1995. Continuum modelling of strong discontinuities in solid mechanics using damage model. *Computational Mechanics* 17, 49–61.
- Ortiz, M., Leroy, Y., Needleman, A., 1987. A finite element method for localized failure analysis. *Computer Methods in Applied Mechanics and Engineering* 61, 189–214.
- Prevost, J.H., Loret, B., 1990. Dynamic strain localization in elasto- (visco-) plastic solids, part 2. Plane strain examples. *Computer Methods in Applied Mechanics and Engineering* 83, 275–294.
- Shawki, T.G., Clifton, R.J., 1989. Shear band formation in thermal viscoplastic materials. *Mechanics of Materials* 8, 13–43.
- Simo, J.C., Oliver, J., Armero, F., 1993. An analysis of strong discontinuities induced by strain-softening in rate-independent inelastic solids. *Computational Mechanics* 12, 277–296.
- Steinmann, P., Willam, K., 1991. Performance of enhanced finite element formulations in localized failure computations. *Computer Methods in Applied Mechanics and Engineering* 90, 845–867.
- Tvergaard, V., 1988. 3D-Analysis of localization failure in a ductile material containing two size-scales of spherical particles. *Engineering Fracture Mechanics* 31, 421–436.
- Watanabe, O., Zbib, H.M., Takenouchi, E., 1998. Crystal plasticity: micro-shear banding in polycrystals using Voronoi tessellation. *International Journal of Plasticity* 14, 771–788.
- Zbib, H.M., Jubran, J.S., 1992. Dynamic shear banding: a three-dimensional analysis. *International Journal of Plasticity* 8, 619–641.